CHAPTER V
EFFECT OF STEAM CONTENT AND O_2 PRETREATMENT ON THE CATALYTIC ACTIVITIES OF Au/CeO_2–Fe_2O_3 CATALYSTS FOR STEAM REFORMING OF METHANOL*

5.1 Abstract

The Au/CeO_2–Fe_2O_3 catalysts prepared by deposition-precipitation were studied on steam reforming of methanol (SRM). Complete methanol conversion was obtained at the optimal steam/methanol ratio of 2 at 400 °C. A high steam content strongly depressed both methanol conversion and hydrogen concentration since this led to a complex mechanism and the formation of carbonate and formate species. After pretreating with oxygen, the catalytic activity dramatically decreased with the presence of an inhomogeneous $Ce_xFe_{1-x}O_2$ solid solution phase; the covering Au sites by the free α–Fe_2O_3 particles; and an agglomeration on both free α–Fe_2O_3 and Au particles.

Keywords: Steam reforming; Methanol; Hydrogen; Carbonate; Formate; Au catalyst

5.2 Introduction

Proton exchange membrane fuel cells (PEMFCs)—a green technology—can generate electricity without emissions by reactions between H_2 and O_2 in the feed [1]. However, the requirement of high H_2 purity feed linking with the performance of the Pt electrode in PEMFC does not allow the amount of CO contamination in the feedstream from H_2 production process to be higher than 10 ppm. To achieve high purity of this energy carrier (H_2), the steam reforming process of liquid hydrocarbon and alcohol fuels was used to provide a suitable feed for PEMFC. Methanol (CH_3OH) has received much attention by virtue of fact that the operating temperature can be as low as 200–400 °C, when compared with other oxygenated compounds and hydrocarbon fuels [2,3]. Normally, the steam reforming of methanol (SRM) is an

*Journal of Industrial and Engineering Chemistry, 20 (2014) 961–971.

endothermic reaction that requires external heat from the surroundings to be favorable at a high temperature. However, CO can be produced as a by-product at high temperature via methanol decomposition (DCM), which depresses the H_2 purity during the SRM [4,5]. In order to improve SRM activity in the low-temperature range, many effective parameters: H_2O/CH_3OH ratio [5], types of catalyst selection [6], catalyst preparation method [7], and reaction temperature [4] are considered.

Among the catalysts studied for H_2 production and CO reduction, one of the most active catalysts is a copper-(Cu-) based catalyst, which exhibits superior catalytic activity; however, the thermal stability is less at T > 270 °C because of its pyrophoric characteristic [8]. Recently, the selection of noble metal catalysts has been developed to be more active, especially for the gold-(Au-) based catalysts which play a role in reducing CO under a low temperature operation via CO oxidation [9] and water-gas shift (WGS) reactions [10]. It has also been found that the high H_2 purity could be achieved by the introduction of Au metal in methanol reforming, and its activity strongly depends on the gold particle size [4,5], method of preparation [11], and type of support [12]. For the metal oxide support selection, ceria (CeO_2) has an oxygen storage capacity, which can store and release active oxygen to achieve good catalytic activity. Besides, the addition of hematite (Fe_2O_3) in the ceria is known to form the solid solution phase ($Ce_xFe_{1-x}O_2$), resulting in an increase in both the oxygen vacancies or storage sites of the support, and its reducibility [13,14]. In 2012, Au supported on CeO_2 and CeO_2–Fe_2O_3 mixed oxides supports exhibited excellent performance in H_2 yield for both oxidative steam reforming of methanol (OSRM) and SRM, while the CO amount was produced in minute amounts [4,5,15]. We have previously reported that our catalyst with a Ce:Fe atomic ratio of 1:1 calcined at 400 °C exhibited good activity for SRM because these conditions provided a homogeneous solid solution (strong Ce–Fe interaction) and strong Au–support ($Au–Fe^{3+}$) interaction [4]. Interestingly, it is well known that the catalytic performance of Au catalysts also depends on the pretreatment conditions and in the presence of O_2, where the Au catalysts exhibit stronger catalytic activity in CO oxidation [16]. The O_2 pretreatment may affect the change of the solid solution phase and interaction of the prepared catalyst, and it might be beneficial for the regeneration step in minimizing coke formation via coke gasification on the spent

catalyst surface [17]. Hence, the investigation on applying gas pretreatment with the physical-chemical changes of the $Au/CeO_2–Fe_2O_3$ catalyst must be necessary.

Not only the catalyst preparation route, but the difference in feed composition also affected the catalytic activity of the catalyst during the SRM reaction. For instance, some authors reported that the carbonate and formate species could block the active sites or Au-metal oxide interface [18,19] and then lower the catalytic performance when the steam content was increased in the feedstream. Similarly, these species were defined as the poisoning substances that deposited and blocked the active sites on the surfaces of Au/CeO_2, $Au/CeO_2–Fe_2O_3$, and $Au–CuO/CeO_2$ catalysts when varying the steam content in OSRM [5,15,20]. In contrast, the positive effect of water or steam addition was proven by Schubert et al. [21] and Costello et al. [22], and the mechanism pathways of formate/or carbonate species linking with the steam addition had been elucidated only on the WGS reaction. On the other hand, another explanation based on the reaction pathways of thermodynamic evaluation had been proposed to clarify the effect of feed concentration instead [1]. In order to better understand, a study on the surface change of the Au catalyst during the steam variation in the SRM feed was needed.

In the present work, we investigated the effects of the H_2O/CH_3OH molar ratio and O_2 pretreatment on the catalytic activity of $Au/CeO_2–Fe_2O_3$ catalysts for SRM. Many characterization techniques—XRF, XRD, TPR, FTIR, FT-Raman, TEM, and TPO—were undertaken to clarify the catalytic properties of the Au catalysts.

5.3 Experimental

5.3.1 Catalyst preparation

For $CeO_2–Fe_2O_3$ support preparation, cerium (III) nitrate hexahydrate ($Ce(NO_3)_3.6H_2O$) (Aldrich), iron (III) nitrate nonahydrate ($Fe(NO_3)_3.9H_2O$) (Aldrich), and Na_2CO_3 (Riedel-de Haen) were mixed with vigorous stirring at 80 °C and pH 8 via the co-precipitation technique. Finally, the precipitate was washed, dried, and calcined in air at 400 °C for 4 h to obtain the $CeO_2–Fe_2O_3$ supports.

For the 3 wt% Au deposition, similar techniques previously described were used [23,24]. The CeO_2–Fe_2O_3 support .(Ce:Fe atomic ratio of 1:1) was suspended in an aqueous solution of $HAuCl_4.3H_2O$ (0.005 M), which was purchased from Alfa AESAR. The suspension was heated at 80 °C and adjusted to the required pH (pH 8) with vigorous stirring using Na_2CO_3. After the resulting solution was stirred for 1 h and cooled to room temperature, the suspension was washed with warm deionized water to eliminate residue ions. The deionized precipitate was dried at 110 °C overnight and calcined in air at 400 °C for 4 h.

5.3.2 Catalyst characterization

The crystal structures of the fresh and spent catalysts were characterized by X-ray diffraction (XRD. JDX-3530) equipped with a CuK_α (1.5406 Å) X-ray source. A generator was operated at 40 kV and 30 mA. Samples were run in a continuous scan mode in the range of 20–90°.

The size and distribution of the Au particles deposited on the supports were directly observed by a transmission electron microscope, TEM (JEOL, JEM 2010), at an accelerating voltage of 200 kV in bright field mode. Before being transferred in the TEM chamber, the samples were dispersed in ethanol and were then dropped onto a copper grid.

An X-Ray fluorescence spectrometer, XRF (AXIOS PW4400) was used to determine the actual surface (Au, Ce, and Fe) composition.

The Fourier transform infrared spectra (FTIR) of the samples were recorded using a Thermo Nicolet Nexus 670 FTIR spectrometer in absorbance mode at 32 scans with a resolution of 4 cm^{-1}. The spectra in the frequency range of 4000 cm^{-1} to 400 cm^{-1} were obtained by using a deuterated triglycerinesulfate detector (DTGS) with a specific detectivity of 1×10^9 cm $Hz^{1/2}$ w^{-1}.

The Fourier transform Raman spectra (FT-Raman) of the samples were recorded using a Perkin Elmer (Spectrum GX) FT-Raman spectrometer using a Nd-YAG laser (1064 nm) in absorbance mode at 2000 scans with a resolution of 16 cm^{-1}. The frequency range of 3500 to 200 cm^{-1} was obtained.

Temperature-programmed reduction (TPR) was employed by using 10 % H_2 in Ar at 30 mL min^{-1} as a reducing gas in a conventional TPR reactor equipped with a thermal conductivity detector. The reduction temperature was raised from 30 °C to 850 °C at a ramp rate of 10 °C min^{-1}.

For the temperature-programmed oxidation (TPO) experiment, approximately 50 mg of the powdered samples was packed in a quartz reactor and a thermocouple was placed at the top of the catalyst layer. The sample was heated from 100 °C with a heating rate of 12 °C min^{-1} to 900 °C under a flow of 2 % O_2/He using a gas flow rate of 30 mL min^{-1}.

5.3.3 Catalytic activity measurements

Catalytic activity measurements were carried out in a fixed-bed reactor containing 100 mg of Au/CeO_2–Fe_2O_3 catalyst. A mixture of water and methanol in a syringe was injected continuously by a syringe pump at a rate of 1.5 mL h^{-1} to a vaporizer to produce a vapor of methanol and steam, which was mixed with the He carrier gas before entering the catalytic reactor. The H_2O/CH_3OH (or S/M) molar ratio was varied proportionally from 1/1 to 4/1. The SRM reaction was conducted at a reaction temperature of 200 °C to 400 °C under atmospheric pressure.

The stability of the prepared catalysts was tested for 10 h. For the O_2 pretreatment, the fresh catalyst was pretreated at a O_2 flow rate of 30 mL min^{-1} at 200 °C for 2 h. The gas hourly space velocity (GHSV) was kept at 21,000 mL/g-cat. h. The product gases (e.g. H_2, CO, CO_2, and CH_4) from the reactor were analyzed both qualitatively and quantitatively by auto-sampling in an on-line gas chromatograph (GC), Agilent 6890N, equipped with a packed carbosphere (80/100 mesh) column (10 ft x 1/8 inch) and a thermal conductivity detector (TCD). The selectivity of each product gas was defined by the mole percentage in the product stream. No methane formation was observed during this study.

5.4 Results and discussion

5.4.1 Catalyst characterization

Table 5.1 shows the chemical and physical properties of the series of $Au/CeO_2–Fe_2O_3$ catalysts. The actual compositions of all prepared catalysts (Au, Ce, and Fe) were almost the same and close to the expected values. In comparison to the lattice constant of the pure CeO_2 support (a_0 = 0.544 nm) with the Au deposition, changes in the lattice constant indicated a solid solution was formed. Generally, for $a_0 < 0.544$, it agrees well with the existence of a solid solution form, where the Fe^{3+} (r = 0.064 nm) has already incorporated into the Ce^{4+} matrix (r = 0.101 nm) [13]. The O_2 pretreated catalyst, showed a higher lattice constant compared to the unpretreated catalyst, attributing to the distortion of the solid solution phase in the mixed oxides support during pretreatment, where the Fe^{3+} segregation from the Ce^{4+} matrix can be more favorable than cooperation. This kind of observation has been reported in our previous work, in terms of various Ce/Fe ratios [4]. After exposure to the reaction, the spent unpretreated catalyst had no change in lattice constant, whereas that of the spent pretreated catalyst seemed to decrease from 0.542 to 0.540, which was close to the value of the solid solution formation. It could be implied that during exposure to the reaction, the adsorbed oxygen molecules (from the O_2 pretreatment) on the catalyst surface might help restructure and/or partially reconstruct the solid solution phase with some complex mechanisms, which were not discussed in detail here.

Table 5.1 Chemical and physical properties of the 3 wt% $Au/CeO_2–Fe_2O_3$ catalysts

Catalyst	Calcination Temperature	Au	Ce	Fe	CeO_2 Crystallite size[a]	Lattice constant[b]	Au crystallite size (nm)	
	(°C)	(wt%)	(wt%)	(wt%)	(nm)	(nm)	d_{111}	d_{200}
3 wt% Au/CeO_2	400	2.74	97.26	-	7.65	0.544	< 5	n.d.[c]
3 wt% Au/Ce1Fe1	400	2.49	61.88	35.63	6.25	0.540	11.87	n.d.
3 wt% Au/Ce1Fe1	400 (O_2 pretreatment)	2.61	61.97	35.42	6.32	0.542	12.92	11.68
Spent 3 wt% Au/Ce1Fe1	400	2.50	61.88	35.62	6.66	0.540	11.94	n.d.
Spent 3 wt% Au/Ce1Fe1	400 (O_2 pretreatment)	2.62	61.98	35.40	7.15	0.540	12.10	n.d.
3 wt% Au/Fe_2O_3	400	2.57	-	97.43	-	-	10.40	n.d.

[a]Mean crystallite sizes were calculated from the average values of CeO_2 plane (111), (220), and (311).

[b]Unit cell parameter calculated from CeO_2 (220) with Bragg's equation.

[c]Not detectable.

The XRD patterns of the catalysts are shown in Fig. 5.1A and B. The strongest diffraction peak of CeO_2 at $2\theta = 28.5°$ represents the fluorite structure [25]. Other positions of weak peaks at 47.47, 56.33, 69.40, and 76.69° correspond to CeO_2 (220), (311), (400), and (331), respectively, for the CuKα (1.5406 Å) radiation observed on CeO_2 and Au/CeO_2 catalysts [18,26]. The diffraction peaks of α–Fe_2O_3 at 33.1, 35.6, 49.4, 54.0, 62.6, and 64.0° represent the hexagonal structure of the hematite planes of (104), (110), (024), (116), (214), and (300), respectively [27,28], while none of the magnetite phase (Fe_3O_4), FeO, and goethite (FeO(OH)) are observed in the unpretreated fresh catalyst (curve c in Fig. 5.1A). The XRD pattern of $Ce_xFe_{1-x}O_2$ (Ce:Fe = 1:1) (curve c in Fig. 5.1A), and the CeO_2 diffraction peaks became broader with lower intensities, compared to those of pure CeO_2, whereas there is an initial appearance of very weak hematite intensities, which could be defined as well-dispersed Fe^{3+} incorporating inside the Ce^{4+} lattice [13]. It was noted that the creation of the mixed phases also resulted in the reduction of CeO_2 crystallite sizes [4], compared to that of Au/CeO_2, since the high CeO_2 crystallinity was directly inhibited by the amorphous structure of Fe_2O_3. Based on the Scherrer equation, no Au (111) peaks at 38.5° were observed on Au/CeO_2, indicating that the minute Au particle size (less than 5 nm, as a limitation of XRD machine) provided perfect dispersion in the support [5]. In contrast, both Au/Fe_2O_3 and Au/CeO_2–Fe_2O_3 samples had a larger Au crystallite size of 10–12 nm, implying that Fe formed an intermetallic bond with Au, and then partially solubilized to form a Au cluster (Au_n, $1 < n < 10$), which improved Au crystallinity [29].

Interestingly, the O_2 pretreatment could improve the crystallinity of both Au (111) and some α–Fe_2O_3 planes [(104) and (110)], as illustrated in Fig. 5.1B. Moreover, new diffraction peaks became detectable, especially for Au (200) at 44.4°; α–Fe_2O_3 (113) at 40.8° and (018) at 57.5°, Fe_3O_4 at 43.2° [30]; and FeO(OH) at 37.1° [27]; attributing to drastic changes in the structural surface of the pretreated catalyst. However, the hematite plane (018) was also observed at 57.5°, representing a lack of solid solution stability due to the generation of free Fe_2O_3 particles. The possible explanation could be that there was generation of more hematite phases, resulting in more intense α–Fe_2O_3 planes since the Fe^{3+} might be more favorable to

reacting with adsorbed oxygen to form Fe_2O_3, including the free Fe_2O_3 particles with less Ce–Fe interaction inside the Ce^{4+} lattice. This was in agreement with the segregation of the free α–Fe_2O_3 particles from the solid solution phase to the catalyst surface, resulting in the increase in the lattice constant. It is evident, from the XRD patterns, that pretreatment also caused phase transformation from hematite to magnetite and goethite, as shown by the presence of the reflection at 43.2° and 37.1°, respectively.

Generally, Fe_2O_3 can be converted to Fe_3O_4 in an H_2 atmosphere [31]; however, the opposite result under oxidative atmosphere was observed in this work. Based on our prediction, we assumed that our prepared $Ce_xFe_{1-x}O_2$ solid solution phase was an unstable phase, so it could be easily converted to unknown FeO_x structures during pretreatment. These FeO_x structures could be continually converted to other compounds via "topotactic transformation" [32], where the reduction or oxidation processes were randomly controlled [33]. Although there was no appearance of FeO in the pretreated sample, we assumed that the FeO_x might be transformed to Fe_3O_4, followed by the partial transformation to the Fe_2O_3 phase. Consequently, some of the remaining Fe_3O_4 phases were detected by XRD. In conclusion, we defined this phenomenon as the loss of homogeneity in the solid solution phase of our catalyst after pretreatment, resulting in the change in lattice parameter. The exact mechanism of the phase transformation was not clarified.

Taking into account the crystallite size of the CeO_2 and Fe_2O_3 diffractions, determined from the Scherrer equation, as shown in Table 5.2, these values can also be related to the change in the CeO_2 and Fe_2O_3 particle sizes. The results indicated that the increasing of both CeO_2 and Fe_2O_3 crystallite size was pronounced after applying the oxygen pretreatment into the fresh catalyst, which was in line with the significant improvement in intensities of the hematite diffractions, where the segregation of the free α–Fe_2O_3 particles or agglomeration of α–Fe_2O_3 particles on the catalyst surface possibly caused the lack of a $Ce_xFe_{1-x}O_2$ solid solution phase. Besides, the actual Au loading was only at 2.61 wt%, which was much less than Fe (35.63 wt%), so these segregated α–Fe_2O_3 particles probably appeared on the catalyst surface, and then easily blocked or covered the exposing surface area to the reaction instead of Au nanoparticles. Thus, the active Au metals

would not be accessible for the steam reforming reaction. With this assumption, these phenomena could happen to CeO_2 particles as well, but the small change of CeO_2 diffractions in both intensity and size was not as effective, when compared with that of α–Fe_2O_3, as illustrated in Fig. 5.1C.

In addition, the Raman spectra of the fresh catalysts with and without pretreatment are compared in Fig. 5.2 in order to explain the impact of gas pretreatment on the $Ce_xFe_{1-x}O_2$ solid solution. The intense band at 473 cm^{-1} was assigned to the F_{2g} symmetric breathing mode of O atoms around each Ce^{4+} in metal oxides with a fluoride structure, and the weak band at 598 cm^{-1} was related to the oxygen vacancies in ceria lattice [34–36]. Furthermore, the bands at 287 and 405 cm^{-1} represented the spectra of α–Fe_2O_3 [34,37]. A small shift towards higher wavenumbers of the α–Fe_2O_3 bands (301 and 419 cm^{-1}) was observed after pretreatment, postulating that the change on the α–Fe_2O_3 part in the mixed oxides was possible. In addition, there was a large difference in the intensities of the CeO_2 bands in both fresh catalysts. It should be pointed out that the gas pretreatment during the preparation step was effective in relation to the amount of oxygen vacancies in the CeO_2–Fe_2O_3. In order to evaluate the concentration of oxygen vacancies in the mixed oxides, the intensity ratio of the bands at 598 and 473 cm^{-1} (I_{598}/I_{473}) was calculated, as shown in Table 5.2. It was clearly seen that the intensity ratio of the fresh catalyst decreased significantly after applying the O_2 pretreatment (0.194 → 0.069), implying that the concentration of the oxygen vacancies in the CeO_2–Fe_2O_3 support was annihilated. This ratio was also attributed to the formation of solid solution, which is known to start with the vacancy compensation mechanism [34,38]. When applying the O_2 pretreatment, less solid solution was formed since it could interrupt this vacancy compensation mechanism by forming free α–Fe_2O_3 particles and Fe^{3+} segregation, resulting in less oxygen vacancies being provided. Even though there are many variable parameters during the catalyst preparation step—types and amounts of dopants in CeO_2–MO_x (M = Fe, Mg, Al, Si, Ga, and Cr) [39,40] and cerium precursor [41]—affecting the concentration of oxygen vacancies in the $Ce_xM_{1-x}O_2$ solid solution, as evidenced by Raman spectra characterization, we

defined the O_2 pretreatment as another necessary parameter in the preparation of the CeO_2–Fe_2O_3 support.

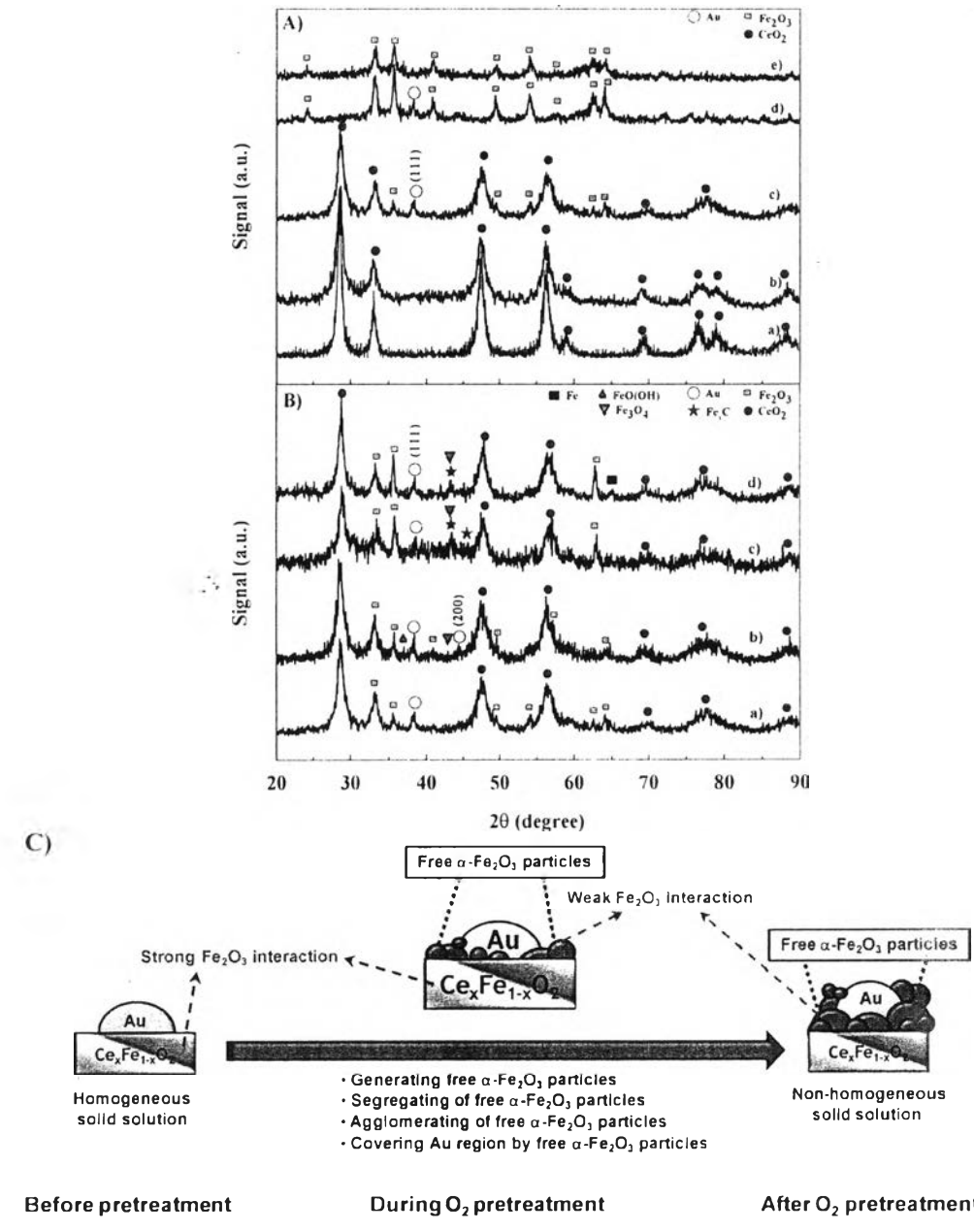

Figure 5.1 XRD patterns of the catalysts: (A) Support and supported Au catalyst; (a) CeO_2, (b) 3 wt% Au/CeO_2, (c) 3 wt% Au/CelFel, (d) 3 wt% Au/Fe_2O_3, and (e) Fe_2O_3. (B) Fresh and spent Au/CeO_2-Fe_2O_3 catalysts; (a) unpretreated fresh catalyst; (b) O_2 pretreated fresh catalyst; (c) unpretreated spent catalyst; and (d) O_2 pretreated spent catalyst. (C) Schematic drawing of the change on the catalyst surface after pretreatment.

In terms of Au structural change after pretreatment, the Au (111) crystallite size increased from 11.9 nm to 12.9 nm and Au (200) crystallite size was also observed at 11.7 nm (curve b in Fig. 5.1B), indicating that Au agglomeration was favored. In contrast to Au/Mn_2O_3, the oxygen pretreatment had a negligible effect on the Au particle size [42]. Although there were many possibilities to identify the dominator for the growth of Au nanoparticles during pretreatment, we focused on the phase transformation of the FeO_x support that could disrupt the Au particles, resulting in the restructure of the Au particles [43]. It has also been reported that pretreatment gas conditions can exert a considerable impact on the structure and activity of the Au catalysts due to enrichment in the Au and O contents on the surface of the catalyst, as evidenced by XPS [44]. In order to support the above statement, TPR and TEM gave useful information for solving this problem.

Table 5.2 Crystallite sizes and the intensity ratio of Raman bands of the fresh 3 wt% Au/CeO_2–Fe_2O_3 catalysts

Catalyst[a]	CeO_2 Crystallite size (nm)				Fe_2O_3 Crystallite size (nm)						I_{598}/I_{473}[b]
	(111)	(220)	(311)	Average	(104)	(110)	(116)	(214)	(300)	Average	
3 wt% Au/CeIFeI	6.10	6.55	6.10	6.25	8.83	12.66	12.94	11.86	8.30	10.92	0.194
3 wt% Au/CeIFeI (O_2 pretreatment)	6.95	5.24	6.77	6.32	9.63	12.73	14.30	12.24	10.34	11.85	0.069

[a]All catalysts were calcined at 400 °C.

[b]Calculated from the intensity ratio of Raman bands at 473 cm^{-1} and 598 cm^{-1}.

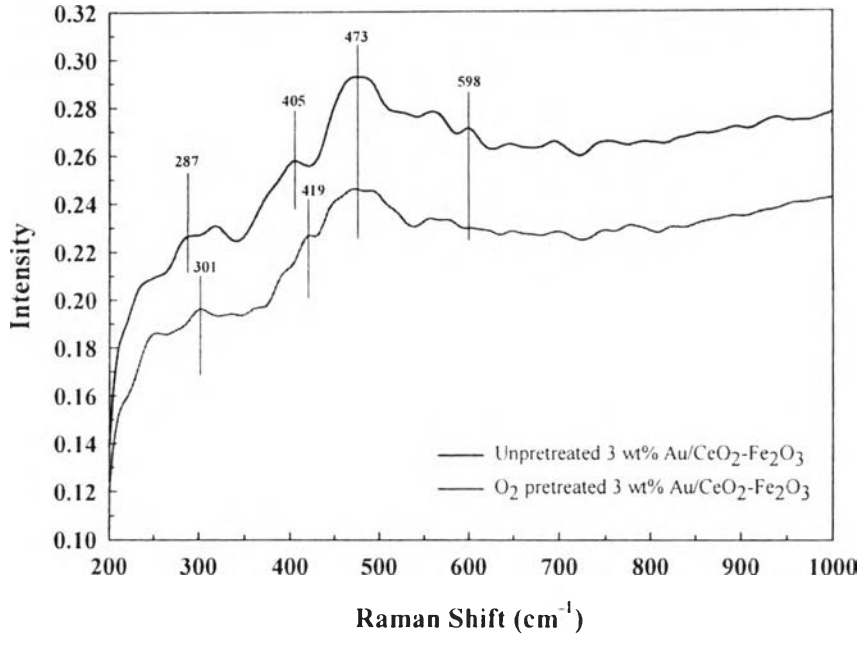

Figure 5.2 Raman spectra of the fresh 3 wt% Au/CeO_2–Fe_2O_3 catalysts with and without O_2 pretreatment.

As seen in the TEM images, Fig. 5.3A and B, an increase in Au particles from 43 nm to 50 nm is observed when catalyst was pretreated. Apparently, there is an agglomeration of Au particles on the pretreated sample, which is in agreement with the XRD patterns, where Au sintering could be related. Even though the change in Au metallic particle size was low, the existence of Au (200) was enough evidence to confirm Au agglomeration in this case.

According to the TPR profiles of the supports (Fig. 5.4), the oxygen surface reduction of the ceria is assigned to the very broad peak located at 489 °C; and another peak at a higher temperature (~850 °C) indicates ceria bulk reduction (CeO_2 to Ce_3O_4) [45]. In the two-step reduction of Fe_2O_3, the first peak at 432 °C represents the hematite-to-magnetite transformation ($Fe_2O_3 \rightarrow Fe_3O_4$), followed by the transformation to metallic iron ($Fe_3O_4 \rightarrow FeO \rightarrow Fe$) at 698 °C [46]. In comparison with the individual supports, the mixed oxides show three reduction peaks: the first peak is assigned to the hematite-to-magnetite state; the second peak could be the overlap of the reduction of Ce^{4+} and the reduction of Fe^{2+}; and the last

peak is attributed to the reduction of bulk CeO_2 [47]. The results reveal that the presence of Fe could enhance reducibility of the catalysts by shifting reduction peaks toward lower temperatures, correlating with the strong Ce–Fe interaction in the $Ce_xFe_{1-x}O_2$ solid solution phase [13,48]. The lowest temperature reduction (114–129 °C) for the $Au/CeO_2–Fe_2O_3$ catalysts (Fig. 5.4 curve d and e) is related to the Au_xO_y reduction and/or Au hydroxide to Au metallic specie (Au^0) [49]. Almost all reduction peaks of the support shifted toward lower temperatures, implying that the deposition of Au improved the reducibility of all supports by strengthening the Au–support (Ce or Fe) interaction [27], after weakening the Fe–O or Ce–O bonding [50].

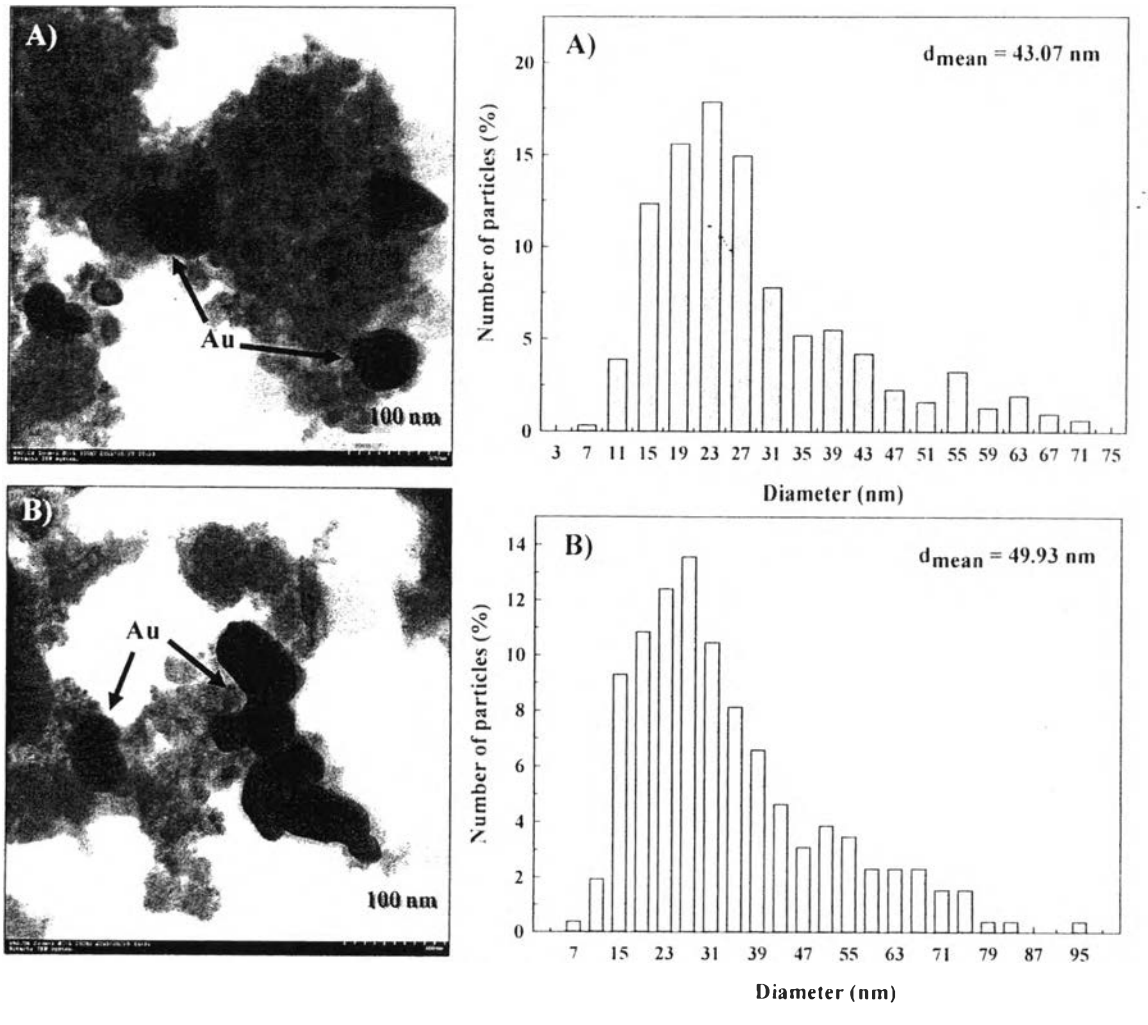

Figure 5.3 TEM images and Au particle size distributions: (a) unpretreated fresh catalyst; and (b) O_2 pretreated fresh catalyst.

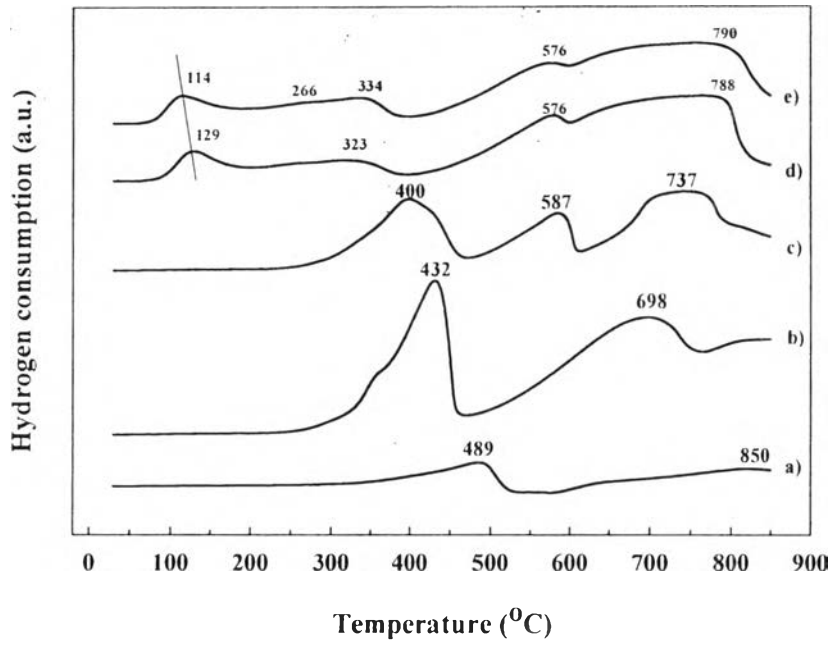

Figure 5.4 TPR profiles of samples calcined at 400 °C: (a) CeO_2; (b) Fe_2O_3; (c) Ce1Fe1; (d) unpretreated fresh 3 wt% Au/Ce1Fe1; and (e) O_2 pretreated fresh 3 wt% Au/Ce1Fe1.

The pretreated fresh catalyst presented two more separation peaks in the solid solution region, which could be classified into two types of hematite interactions; (i) larger free α–Fe_2O_3 particles, corresponding to lower Ce–Fe interactions (or strong Fe–Fe interactions) at a very broad peak of the lower reduction temperature at 266 °C and (ii) small Fe_2O_3 particles with strong Ce–Fe interactions, contributing to a higher reduction temperature of 334 °C. The results revealed that the adsorbed oxygen might interact with the Fe^{3+} in the $Ce_xFe_{1-x}O_2$ support to form more free Fe_2O_3 particles, so that segregation of Fe^{3+} from the solid solution region could be attained. Similar to our previous work, the same existence of free Fe_2O_3-type particles was also observed in calcination temperatures lower than 400 °C, and defined as the main factor for providing an inhomogeneous solid solution phase in the CeO_2–Fe_2O_3 support [4]. A different kind of free particle has already been reported in another type of catalyst as well. For instance, the NiO/CeO_2–ZrO_2 catalyst has free NiO particles with less metal–support interaction

[51], while our results displayed free α–Fe_2O_3 particles with less support–support interaction. The shifting peak of Au_xO_y species toward a lower temperature (129 °C to 114 °C) could be attributed to either lower metal–support interaction or higher metal–metal interaction of Au_xO_y particles, indicating that the Au agglomeration effect was more pronounced and resulted in a larger Au particle size (50 nm). These results were in line with the XRD and TEM results.

In the FTIR spectra, shown in Figure 5.5A–C, the appearance of the formate and carbonate species (or the adsorbed reaction intermediates), including the hydroxyl group are clearly observed on the surfaces of the spent catalysts with various H_2O/CH_3OH molar ratios as follows: (A) carbonate at 1200 cm^{-1} to 1700 cm^{-1}, (B) formate at 2800 cm^{-1} to 3000 cm^{-1}, and (C) hydroxyl at 3200 cm^{-1} to 3600 cm^{-1}. Many types of carbonate and formate species are detected in many positions, including abundant unspecified carbonate species. It is noted that the difference in formate and carbonate species is a consequence of the type of reaction and the type of used catalyst [18]. However, the bands at 2343 and 2360 cm^{-1} could be related to the band of CO_2 adsorbed species, which probably originates from the reaction between the oxygen molecules during the reoxidation of ceria and the CO adsorbed species during the reaction [52]. In consideration of the possible routes of carbonate formation (1340–1344 cm^{-1} and 1525–1550 cm^{-1} [52,53]) on the catalyst surface, the first route might be the dehydration of the surface bicarbonate intermediate ($-CO_3H$, assigned at 1590, 1390, and 1212 cm^{-1}) [52,53] and an adjacent hydroxyl (OH^-) [54]. The second route might be the adsorption of CO_2 which is the reaction product at the catalyst surface, and this route has been proposed in the Au/CeO_2 catalyst during the WGS reaction [52,53]. In contrast, the route of formate formation is attributed to the reaction between CO adsorbed on the $Au^{\delta-}$ and OH groups located on the Ce^{x+} of the ceria surface [55], as evidenced in the strongest bands at 2853 cm^{-1}, and at 2924 cm^{-1} and 2955 cm^{-1} relating to the formate species on Ce^{3+} and Ce^{4+} [18,52], respectively.

Furthermore, the change in both carbonate and formate intensities was observed with S/M variation. The formate intensities proportionally increased when increasing the S/M from 1/1 to 3/1. This was in line with previous works [56,57] that stated that higher formate contents originated from the high steam addition in the

reaction. Likewise, the intensities of the carbonate species (1344 and 1525 cm^{-1}) also followed the same trend as those of the formate species. We speculated that the trends of these species related to the routes of the formation of each species in the presence of the steam addition. In addition, all of these specified species implied that the blocking of the active sites on the Au catalyst by the carbonate and formate was possible with the steam variation in the SRM.

Except for the spent catalyst at the highest S/M of 4/1, the overall carbonate intensities became weaker, while the formate and CO_2 adsorbed bands increased. The decrease in carbonate species by the addition of high steam content (S/M = 4/1) possibly came from the carbonate decomposition, known as reversed carbonate formation, by heated water [54,58]. In some cases, the positive effect of the steam addition was to lower the carbonate species that blocked the active sties of some catalysts, such as Pd/CeO_2 [59], Au/CeO_2 [5], and $Au–CuO/CeO_2$ [20]. Another pathway in the reverse carbonate formation was that the carbonate might potentially be converted to a less stable bicarbonate by steam, and then continually changed to CO_2 adsorbed species [60]. The above statements agree well with our results, and we speculated that the $Au/CeO_2–Fe_2O_3$ catalysts were, at least, similarly affected by the carbonate and formate species in the presence of steam variation. However, the exact mechanisms of these phenomena were still unclear.

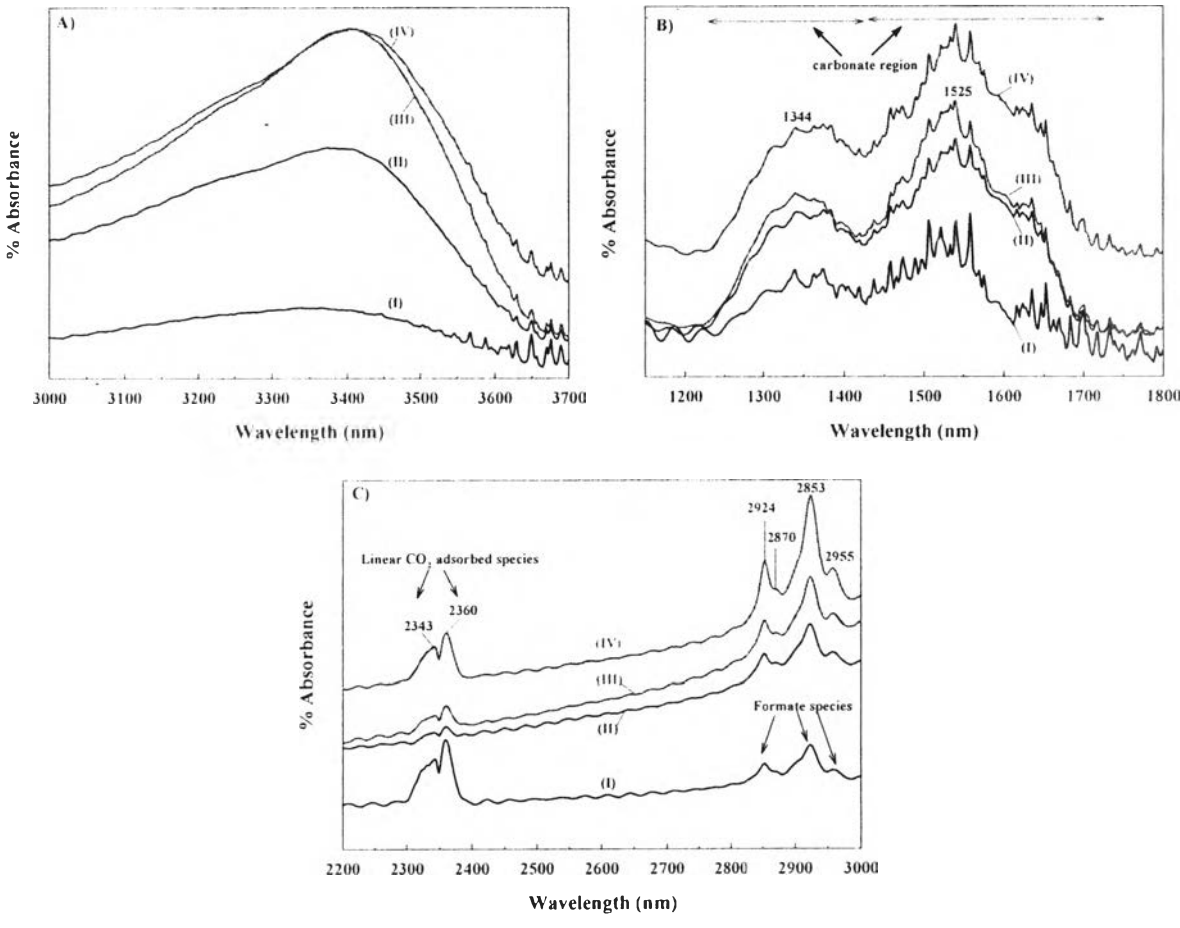

Figure 5.5 FTIR spectra of 3 wt% Au/CeO_2–Fe_2O_3 catalysts: (a; 3000–3700 cm^{-1}, b; 1150–1800 cm^{-1}, and c; 2200–3000 cm^{-1}) (I) after reaction at H_2O/CH_3OH molar ratio of 1/1; (II) after reaction at H_2O/CH_3OH molar ratio of 2/1; (III) after reaction at H_2O/CH_3OH molar ratio of 3/1; and (IV) after reaction at H_2O/CH_3OH molar ratio of 4/1.

5.4.2 Catalytic activity

5.4.2.1 Effect of O_2 pretreatment

There are many findings regarding the effect of pretreatment, especially O_2 pretreatment. These studies propose that O_2 adsorption proceeds directly on the Au particles, resulting in increased catalytic activity of Au catalysts [61]. In this work, we compared the activity of O_2 pretreated catalyst and the fresh catalyst and expected that after O_2 pretreatment there would be a change taking place at the perimeter of the Au–support.

As illustrated in Fig. 5.6, the negative effect on the catalytic activity from the SRM is observed when the O_2 pretreatment is applied to the fresh Au/CeO_2–Fe_2O_3 catalyst. The methanol conversion and H_2 concentration of the pretreated fresh catalysts are much lower than those of unpretreated fresh catalyst in the range of reaction temperatures (200–400 °C). It is evident from the XRD patterns that O_2 pretreatment causes a significant increase in intensity of hematite, as shown by the reflections at 33.1°, 35.6°, 40.8°, and 57.5°. This suggests that the active solid solution phase changes to various inactive phases (free hematite with less Fe^{3+} interaction, magnetite, and goethite), followed by blocking and/or covering the reaction region of Au sites by these inactive phases, which more severely affected the SRM activity than the Au agglomeration. In some cases, only the inactive Fe_2O_3 phase in Au/FeO_x could inhibit the catalytic activity when the Fe_3O_4 was oxidized into Fe_2O_3 form during air pretreatment [30].

Focusing on the gold structural change, the pretreatment atmosphere significantly influenced: the physical size (geometric effect) and distribution of the gold nanoparticles, electronic effect, gold nature species, and gold–support interaction [30]. When we considered the area under the TPR peak of Au reduction, it only indicated qualitatively that there were (some) $Au^{\delta+}$ species contained in the prepared catalysts. As imaged by TEM, the Au particles represented the existence of Au^0 or Au metallic species for both samples. It is thus assumed that these samples contained both metallic and positively charged Au species. Only the Au particle size exhibited a change to a larger size, where the calculated values could be evidenced. Geometrically, change was another decisive factor because the larger Au particle size caused blocking of the active surface area of the catalyst [5], then catalytic performance was inhibited. It has been reported that the evolution of Au structural growth could be affected by O_2 pretreatment, where the complex model possibly involved the diffusion of Au to the outer surface of the oxide support [35,62]. Other researchers also proposed an evaporation–deposition mechanism during pretreatment of Au/SiO_2, starting with the evaporation of Au particles in the gas phase, resulting in the nucleation of Au atoms in the gas phase, where they then deposited onto the support. Finally, there was an agglomeration of Au clusters [62].

It was further reported that not only the size of Au was changed in this mechanism, but also the dispersion of the Au nanoparticles was improved, indicating the key to high activity in CO oxidation. Nonetheless, our catalyst exhibited poor activity after applying O_2 pretreatment due to the large size of the Au particles and the phase transformation in the support. As a consequence, it is noteworthy that the change of support interaction in the solid solution phase, phase transformation of support, occupying area of reaction sites, and Au particle size were the major factors for effectively providing less active Au catalysis during pretreatment.

The H_2 and CO concentrations were decreased dramatically after the pretreatment of the Au catalyst with oxygen. A range of H_2 concentrations was observed for non-pretreatment and pretreatment fresh catalysts at 10–40 % and 0–32 %, respectively. In addition, both samples showed low values of CO concentration in the range of 0–3 % at the operating temperature of 200 °C to 400 °C. These results may also be related to the existence of Au agglomeration and the lack of homogeneous solid solution due to free α–Fe_2O_3 particle segregation. When interpreting our results, the value of CO concentration was still in the acceptable range for operating at 300 °C in the methanol fuel processor, where the reaction temperature was not too high and the CO concentration was lower than 1 % (< 10,000 ppm) in the presence of rich H_2 concentration (37 %). In comparison with a previous work, our catalysts (Au/CeO_2–Fe_2O_3) seemed to be more active than the precious metal [63], in terms of obtaining the minute amount of CO formed during SRM, before continually sending this reformate to the PROX unit in the methanol fuel processor.

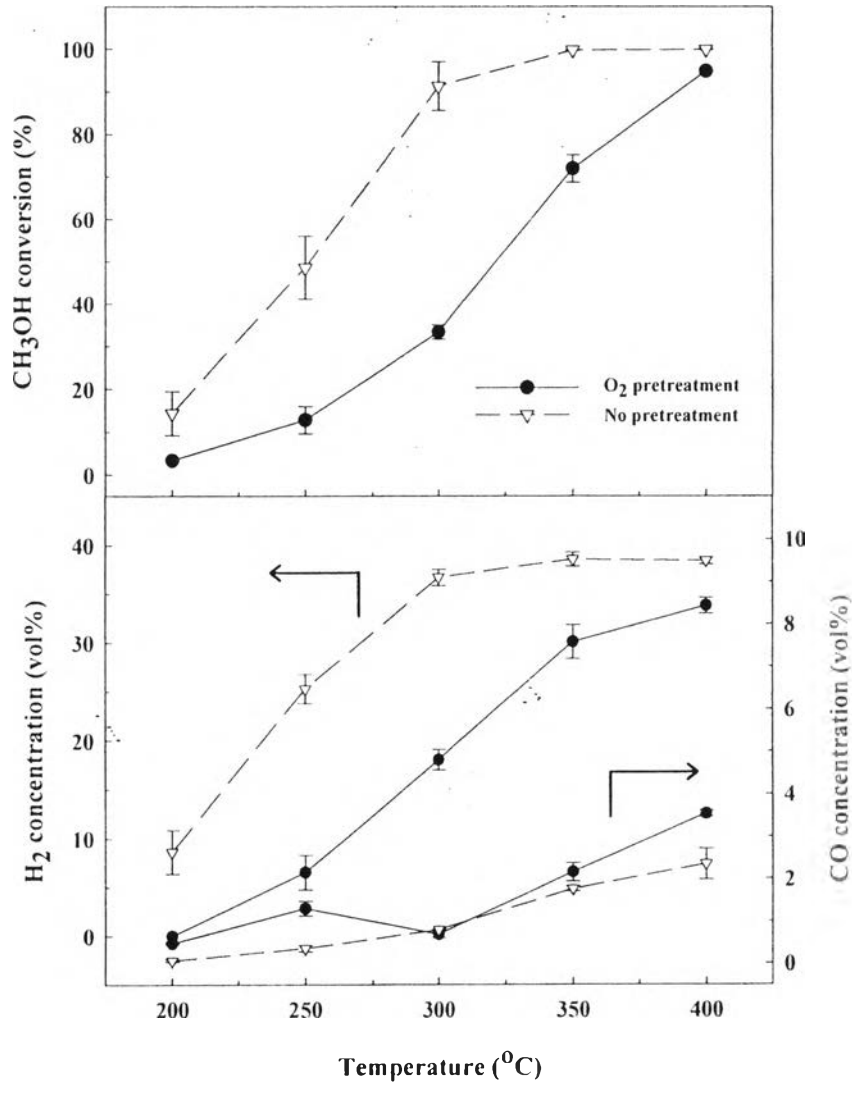

Figure 5.6 Effect of gas pretreatment on methanol conversion and product composition over $Au/CeO_2–Fe_2O_3$. (Reaction conditions: H_2O/CH_3OH, 2/1; calcination temperature, 400 °C.)

5.4.2.2 Effect of H_2O/CH_3OH molar ratio

Figure 5.7 shows the catalytic activities of $Au/CeO_2–Fe_2O_3$ catalysts with various H_2O/CH_3OH (S/M) molar ratios. The lowest catalytic activity is observed on S/M at 1/1 where the amounts of adsorbed species (Fig. 5.5) are also the lowest values, when compared to other S/M ratios. It could be implied that with an insufficient steam addition, the catalysts could not longer undergo an efficient SRM reaction when compared to the higher steam addition. The S/M of 2/1, which

gives the highest methanol conversion and hydrogen yield, is recommended as the optimum condition. When comparing the FTIR results, a higher S/M ratio (S/M > 2/1) resulted in lower catalytic activity caused by the existence of carbonate and formate species, which blocked the active sites of the Au catalyst, as reported elsewhere [5,20]. In addition, Kim and coworkers (2005) proposed that the variation of water pressure could result in the desorption of surface carbonates, known as poisoning by-products for the CeO_2 support. These species could inhibit the catalytic performance of the catalyst [18]. Although a decrease in carbonate species, with increasing formate species, was found at the highest steam contents (S/M = 4/1), the SRM activity lowered progressively. It could be implied that the formate species might negatively affect the SRM activity more than the carbonate species.

Taking into account the product distribution, the H_2 concentration increased with increasing reaction temperatures where the endothermic reaction was favorable; however, the maximum H_2 concentration of 38 % was observed at 400 °C with the S/M of 2/1. The variation of S/M revealed that the H_2 concentration was significantly improved in the range of the initial ratio (1/1–2/1), and was then decreased proportionally when the S/M was higher than the optimum condition. This was in agreement with the previous explanation of carbonate and formate formation, where the Au catalyst deactivated during H_2 production. Similar to the trends of the H_2 concentration, the CO concentration also increased with increasing reaction temperatures since the appearance of a methanol decomposition (DM) reaction might be favored. Indeed, the positive aspect of S/M variation could be discussed in terms of CO reduction, where the CO formation decreased with increasing S/M. Even though the overall CO concentration was still in the minute range at 0–3 %, the addition of steam seemed to help reduce CO content via the WGS reaction during the DM and SRM reaction. The S/M of 2/1 was selected as the optimum condition, where the H_2 concentration was the highest and the low CO concentration was still in the acceptable range for directly sending to the PROX unit in the methanol fuel processor without setting more additional units.

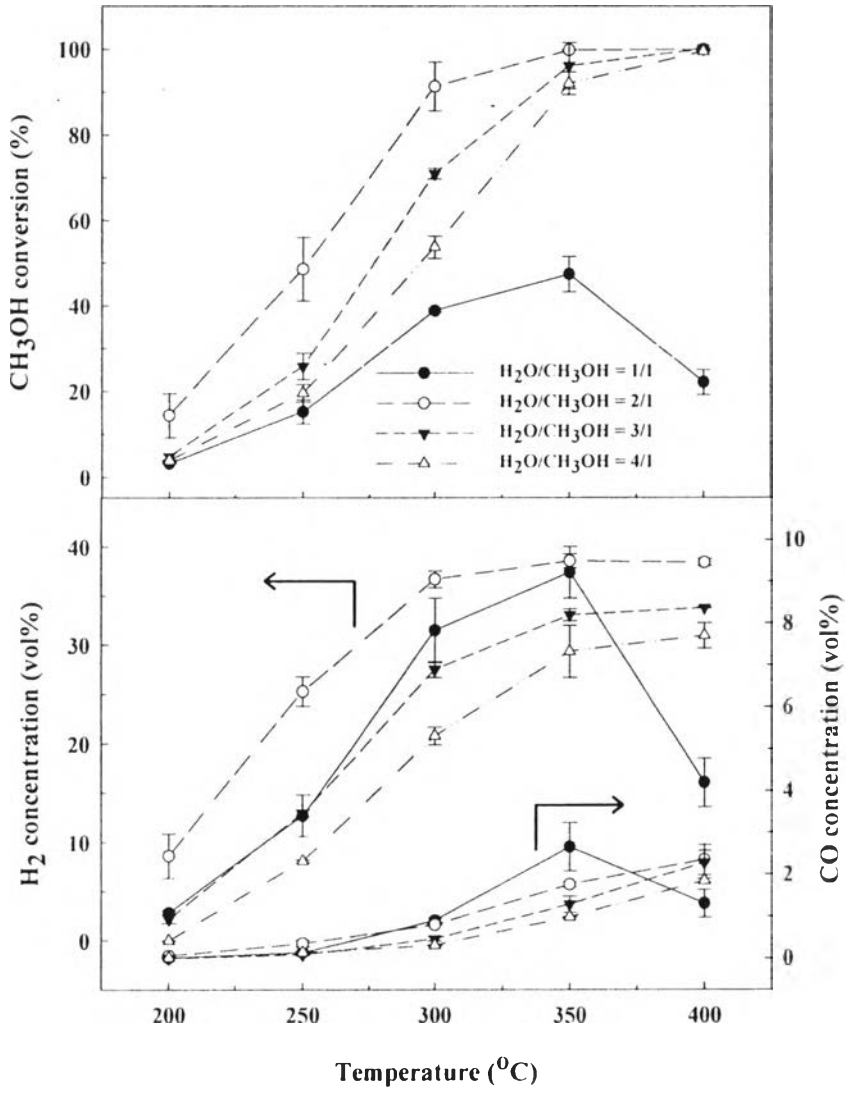

Figure 5.7 Effect of H_2O/CH_3OH molar ratio on methanol conversion and product composition over Au/CeO_2–Fe_2O_3 calcined at 400 °C.

5.4.3 Stability testing

In this experiment, the pretreated and unpretreated fresh Au/CeO_2–Fe_2O_3 catalysts were investigated at 400 °C for 640 min, as shown in Fig. 5.8. The rapid deactivation of the unpretreated catalyst was seen. The methanol conversion and H_2 yield drastically dropped after 1.5 h (~90 min) from 100 % and 74 % to 25.9 % and 19.3 %, respectively. In comparison with the pretreated one at the same 1.5 h of time on stream, better stability of the pretreated catalyst seemed to be observed in

the slower reduction in both methanol conversion (95 → 67.7 %) and H_2 yield (71.3 → 51.7 %). Moreover, at the end of the experiment, higher values of methanol conversion at 47 % and H_2 yield at 35 % were measured. In terms of product selectivity, there was no difference in both types of catalysts; H_2 = 75 %, CO_2 = 17–20 %, and CO = 5–8 %. As mentioned above, the positive effect on the stability of the catalyst could be achieved by O_2 pretreatment, which was necessary for longer thermal stability of the Au/CeO_2–Fe_2O_3 catalyst. Based on our knowledge, carbon or coke deposition normally plays an important role in deactivating a catalyst during a reaction [18], which was similarly reported in our previous works [4,5]. However, we assumed that the adsorbed O_2 molecules on the fresh catalyst surface, after pretreatment, probably also reacted with the coke depositing on the catalyst surface with various complex mechanisms, which could be an explanation for stability improvement. To support this assumption, the TPO technique was necessary for evaluating the change in the amount of coke formed on the spent catalysts. It was found that the amount of coke deposition on the oxygen pretreated catalyst surface was decreased to 0.85 wt%, when compared to that of unpretreated catalyst (2.60 wt%). This was probably due to the diminishment of coke from the catalyst surface in the presence of oxygen via coke gasification, in which two sources of oxygen: (i) oxygen gas introduced into the reaction and (ii) oxygen atom adsorbed in the high oxygen vacancies support could be involved in either Au-based catalysts or $Cu/CeO_2/Al_2O_3$ catalysts [17]. Besides, the deactivated catalysts were also subsequently regenerated with the on-line treatment in O_2 (200 °C for 2 h) in order to check whether the decrease in the amount of coke deposition was still favored or not. As expected, the amount of carbon deposit was decreased to the lowest value of 0.60 wt%, which most likely confirmed the existence of coke gasification during the regeneration step.

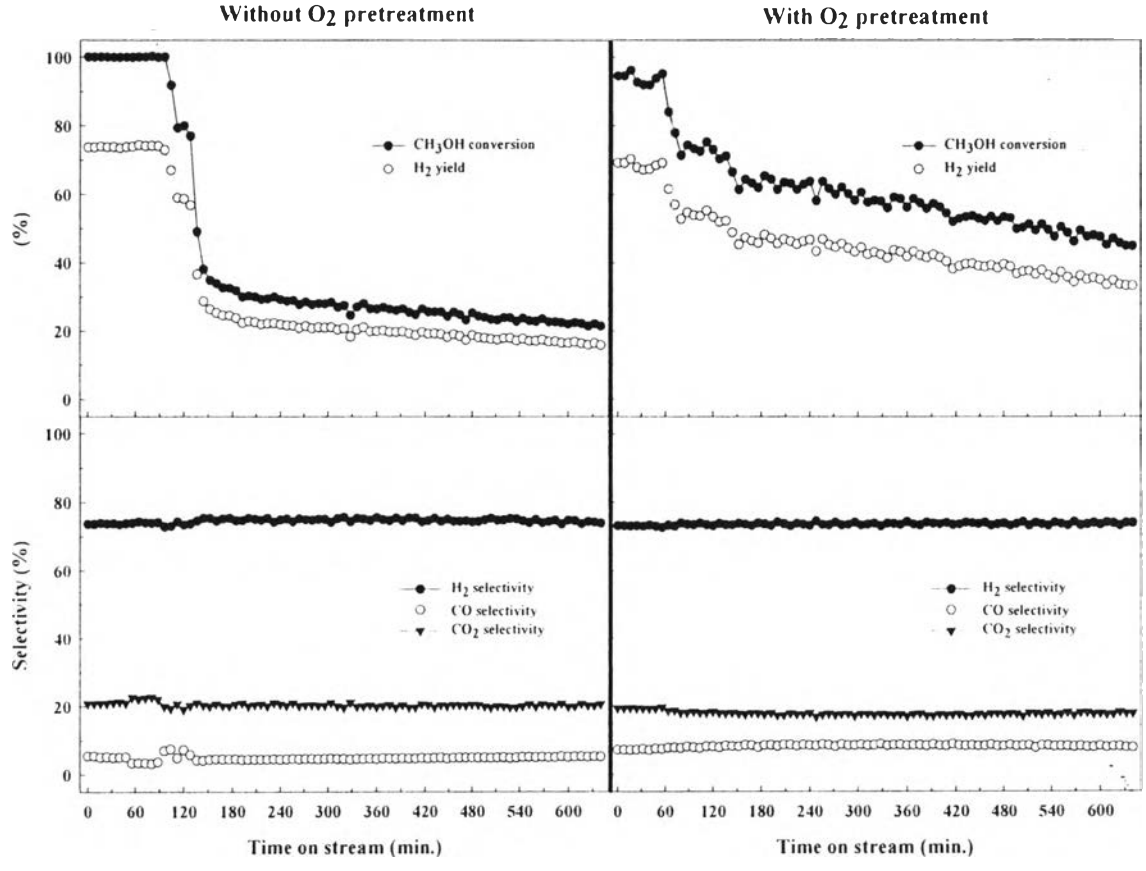

Figure 5.8 Stability observation of the fresh 3 wt% Au/CeO_2–Fe_2O_3 catalysts with and without O_2 pretreatment. (Reaction conditions: H_2O/CH_3OH, 2/1; reaction temperature, 400 °C; and time-on-stream per sample, 640 min.)

According to the TPO profile, the coke deposited on the spent catalyst surface presented two distinct peaks of carbon oxidation, indicating the different positions of coke interactions, as seen in the TPO profiles in Fig. 5.9. For example, the low-temperature oxidations at 285, 312, and 320 °C could be assigned to the oxidation of the poorly polymerized coke deposited on the metal particles, and the high-temperature oxidations at 492, 512, and 593 °C are attributed to the highly polymerized coke deposited near the metal–support interphase [64]. The types of coke formed on the catalyst surface have been previously classified based on the reaction temperature and the type of reaction [65]. In addition, the evaluation of the sources of coke formed has been done previously [1,66]. Depending on the area and intensity of each peak, the results reveal that the amount of low polymerized coke is

higher than that of the highly polymerized coke. For the fresh catalyst, the lowest oxidation temperature at 106 °C can be attributed to the carbonates species [8], where no carbonaceous species were observed. Among the samples studied, the lowest intensity low-temperature oxidation peak was observed in the spent catalyst from the regeneration step, while there was no difference in that of the high-temperature oxidation peak. This confirmed the existence of coke gasification, where the amount of carbon deposits was decreased to the lowest value of 0.60 wt%.

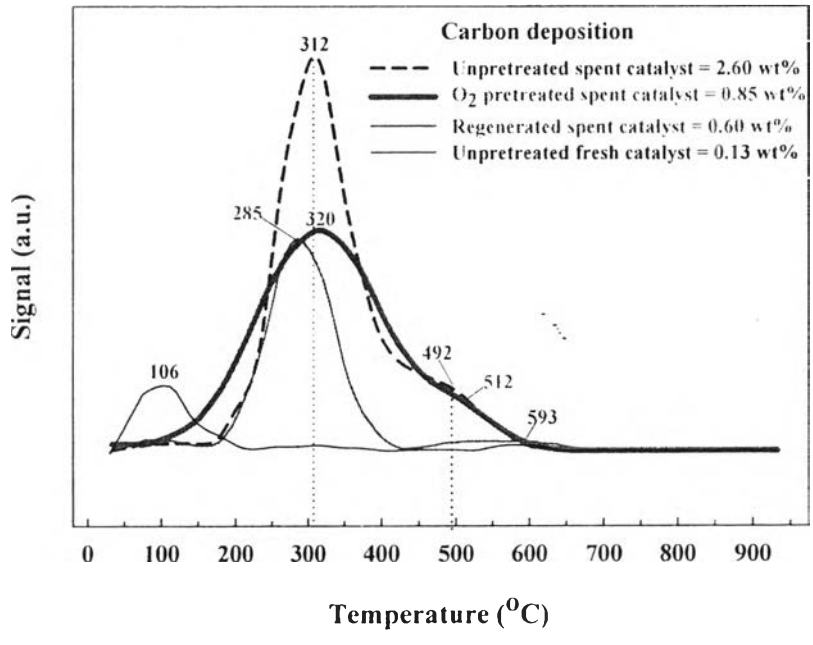

Figure 5.9 TPO profiles of spent 3 wt% $Au/CeO_2–Fe_2O_3$ after exposure to reaction. (Reaction conditions: H_2O/CH_3OH, 2/1; reaction temperature, 400 °C; and time-on-stream per sample, 640 min.)

The XRD patterns of the spent catalysts are also presented in Fig. 5.1B (c,d). Both unpretreated and pretreated spent catalysts presented a decrease in CeO_2 diffraction intensities and the disappearance of some $\alpha–Fe_2O_3$ diffraction peaks, implying that the coke partially covered both the metal and support surfaces. In addition, the crystallinity of some angles of α-Fe_2O_3 (at 35.6° and 62.6°) seemed to be improved, which possibly came from sintering of Fe_2O_3 particles and/or the segregation of Fe_2O_3 from the homogeneous solid solution during the stability test.

Likewise, the peaks of iron (Fe), which might come from sintering and/or the reduction process of Fe_2O_3, and carbon iron chemical compounds (Fe_xC) were also introduced. The appearance of Fe_xC confirmed that coke remained on the spent catalyst surface. To support the above explanation, Knogzhai et al. also defined Fe_3C as the source of massive carbon deposits on the spent catalyst, as detected by XRD [67]. Particularly, the Fe_3O_4 diffractions (43.2°) also appeared close to Fe_xC, where those peaks overlapped. Taking into account the phase transformation of Fe_2O_3 to Fe_3O_4, it was identified that the hematite in the solid solution phase could be reduced to the less active magnetite phase during the reaction. This reduction behavior was in accordance with Kudo et al., who found the same transformation in Au/Fe_2O_3 during the WGS reaction and indicated that the amounts of H_2 consumed in the reduction process were performed or spilled over the iron oxide surface stoichiometrically using the following equation: $Fe_2O_3 + 1/3H_2 \rightarrow 2/3Fe_3O_4 + 1/3H_2O$, where H_2 came from the product streams in the gas phase [68]. They also inferred that the existence of Au/Fe_3O_4 seemed to provide a catalytically active oxidation state in WGS, whereas our work defined this reduced state as the inactive phase for SRM. When compared with the CeO_2 diffraction peaks in the spent catalysts, the intensities of the spent pretreated catalyst became more pronounced. This was also evidenced by coke gasification resulting in reduced coke deposition on the CeO_2 surface. Consequently, the intensities of the CeO_2 peaks were then higher than those of the unpretreated spent catalyst.

According to the Au diffractions of the spent catalysts, no improvement in intensity or Au (111) crystallite size (11–12 nm) was observed, indicating that Au sintering did not occur during the stability test. Additionally, Au (200) disappeared with the presence of less Au (111) intensity in the spent catalyst, implying that not only the coke, but some of the segregated α–Fe_2O_3 particles on the outer catalyst surface also partially covered the Au surface, which was not accessible to the reaction during stability test. This could be one of the causes of the short life of the Au/CeO_2–Fe_2O_3 catalyst.

5.5 Conclusions

It can be concluded that the highest catalytic activity of 3 wt% Au/CeO_2–Fe_2O_3 (Ce:Fe = 1:1) catalyst could be obtained when an optimum amount of steam was added to the reaction in order to avoid the inhibition of carbonate and formate species. The effect of O_2 pretreatment did not improve the uniform solid solution of $Ce_xFe_{1-x}O_2$ in the fresh catalyst, but it was necessary for coke removal from the spent catalyst during regeneration. Coke formation and the phase change in the support were the main causes of catalyst deactivation, which were confirmed by XRD and TPO techniques. Nonetheless, no Au sintering was observed during the stability test. As our limitation, we were not able determine the exact amounts of Au species (Au^0 and $Au^{\delta+}$) in this experiment. In terms of product distribution, the Au/CeO_2–Fe_2O_3 catalyst will be useful for providing H_2-rich reformate in the low temperature zone (300 °C) before sending to the PROX in the practical methanol fuel processor, in which further experiments to be carried out in the future.

5.6 Acknowledgements

The authors acknowledge the contributions and financial support of the following organizations: the Thailand Research Fund through the Royal Golden Jubilee Ph.D. Program (Grant No. PHD/0282/2552); the Center of Excellence on Petrochemicals and Materials Technology, Chulalongkorn University; and The National Research University Project of CHE and the Ratchadaphiseksomphot Endowment Fund (EN276B).

5.7 References

[1] K. Faungnawakij, R. Kikuchi, K. Eguchi, J. Power Sources 161 (2006) 87–94.

[2] R. Pérez-Hernández, A. Gutiérrez-Martínez, J. Palacios, M. Vega-Hernández, V. Rodríguez-Lugo, Int. J. Hydrogen Energy 36 (2011) 6601–6608.

[3] R. Pérez-Hernández, A. Gutiérrez-Martínez, C.E. Gutiérrez-Wing, Int. J. Hydrogen Energy 32 (2007) 2888–2894.

[4] C. Pojanavaraphan, A. Luengnaruemitchai, E. Gulari, Int. J. Hydrogen Energy 37 (2012) 14072–14084.

[5] C. Pojanavaraphan, A. Luengnaruemitchai, E. Gulari, Chem. Eng. J. 192 (2012) 105–113.

[6] T.J. Huang, H.M. Chen, Int. J. Hydrogen Energy 35 (2010) 6218–6226.

[7] P. Bichon, M. Asheim, A. Jordal, T. Sperle, M. Fathi, A. Holmen, E.A. Blekkan, Int. J. Hydrogen Energy 32 (2007) 1799–1805.

[8] N. Yi, R. Si, H. Saltsburg, M.F. Stephanopoulos, Appl. Catal., B 95 (2010) 87-92.

[9] A. Luengnaruemitchai, D.T.K. Thoa, S. Osuwan, E. Gulari. Int. J. Hydrogen Energy 30 (2005) 981-987.

[10] A.A. El-Moemen, G. Kučerová, R.J. Behm, Appl. Catal., B 95 (2010) 57–70.

[11] M. Jia, X. Li, Zhaorigetu, Y. Shen, Y. Li, J. Rare Earths 29 (2011) 213–216.

[12] M. Meng, Y. Tu, T. Ding, Z. Sun, L. Zhang, Int. J. Hydrogen Energy 36 (2011) 9139–9150.

[13] T. Tabakova, G. Avgouropoulos, J. Papavasiliou, M. Manzoli, F. Boccuzzi, K. Tenchev, F. Vindigni, T. Ioannides, Appl. Catal., B 101 (2011) 256–265.

[14] T. Tabakova, M. Manzoli, D. Paneva, F. Boccuzzi, V. Idakiev, I. Mitov, Appl. Catal., B 101 (2011) 266-274.

[15] U. Satitthai, A. Luengnaruemitchai, E. Gulari, Int. J. Chem. Biolog. Eng. 6 (2012) 322–327.

[16] R.R. Zhang, L.H. Ren, A.H. Lu, W.C. Li, Catal. Commun. 13 (2011) 18–21.

[17] S. Patel,K.K. Pant, Fuel Process. Technol. 88 (2007) 825–832.

[18] C.H. Kim, L.T. Thompson, J. Catal. 230 (2005) 66–74.

[19] M.M. Schubert, V. Plzak, J. Garche, R.J. Behm, Catal. Lett. 76 (2001) 143–150.

[20] P. Pipatpratanporn, MS. Thesis 2011, The Petroleum and Petrochemical College, Chulalongkorn University, Bangkok.

[21] M.M. Schubert, A. Venugopal, M.J. Kahlich, V. Plzak, R.J. Behm, J. Catal. 222 (2004) 32–40.

[22] C.K. Costello, M.C. Kung, H.S. Oh, Y. Wang, H.H. Kung, Appl. Catal., A 232 (2002) 159–168.

[23] K. Y. Ho, K.L. Yeung, Gold Bull. 40 (2007) 15–30.

[24] K. Y. Ho, K.L. Yeung, J. Catal. 242 (2006) 131–141.

[25] G. Neri, A. Bonavita, G. Rizzo, S. Galvagno, S. Capone, P. Siciliano, Sens. Actuators, B 114 (2006) 687–695.

[26] J. Kunming, Z. Huili, L. Wencui, Chin. J. Catal. 29 (2008) 1089–1092.

[27] F.W. Chang, L.S. Roselin, T.C. Ou, Appl. Catal., A 334 (2008) 147–155.

[28] X.C. Jiang, A.B. Yu, J. Mater. Process. Technol. 209 (2009) 4558–4562.

[29] D. Andreeva, T. Tabakova, V. Idakiev, P. Christov, R. Giovanoli, Appl. Catal., A 169 (1998) 9–14.

[30] J. Huang, W.L. Dai, K. Fan, J. Catal. 266 (2009) 228–235.

[31] G. Munteanu, L. Ilieva, D. Andreeva, Thermochim. Acta 291 (1997) 171–177.

[32] P. Becker, J.J. Heizmann, R. Baro, J. Appl. Crystallogr. 10 (1977) 77–78.

[33] C.J. Jia, L.D. Sun, Z.G. Yan, Y.C. Pang, L.P. You, C.H. Yan, J. Phys. Chem. C 111 (2007) 13022-13027.

[34] H. Bao, X. Chen, J. Fang, Z. Jiang, W. Huang, Catal. Lett. 125 (2008) 160–167.

[35] J.R. McBride, K.C. Hass, B.D. Poindexter, W.H. Weber, J. Appl. Phys. 76 (1994) 2435–2441.

[36] K. Li, H. Wang, Y. Wei, D. Yan, Chem. Eng. J. 156 (2010) 512–518.

[37] D.L. De Faria, S.V. Silva, M.T. De Oliveira, J. Raman Spectrosc. 28 (1997) 873–878.

[38] A. Trovarelli, Comments Inorg. Chem. 20 (1999) 263–284.

[39] L. Minervini, M.O. Zacate, R.W. Grimes, Solid State Ionics 116 (1999) 339–349.

[40] Q. Yu, X. Wu, C. Tang, L. Qi, B. Liu, F. Gao, K. Sun, L. Dong, Y. Chen, J. Colloid Interface Sci. 354 (2011) 341–352.

[41] L. Liu, Y. Cao, W. Sun, Z. Yao, B. Liu, F. Gao, L. Dong, Catal. Today 175 (2011) 48–54.

[42] L.C. Wang, L. He, Y.M. Liu, Y. Cao, H.Y. He, K.N. Fan, J.H. Zhuang, J. Catal. 264 (2009) 145–153.

[43] L.F. Allard, A. Borisevich, W.L. Deng, R. Si, S.M. Flytzani, S.H. Overbury, J. Electron Microsc. 58 (2009) 199–212.

[44] S.D. Gardner, G.B. Hoflund, B.T. Upchurch, D.R. Schryer, E.J. Kielin, J. Schryer, J. Catal. 129 (1991) 114–120.

[45] G. Jacobs G, U.M. Graham, E. Chenu, P.M. Patterson, A. Dozier, B.H. Davis, J. Catal. 229 (2005) 499–512.

[46] A. Venugopal, M.S. Scurrell, Appl. Catal., A 258 (2004) 241–249.

[47] L. Kongzhai, W. Hua, W. Yonggang, Y. Dongxia, Int. J. Hydrogen Energy 36 (2011) 3471–3482.

[48] F.J.P. Alonso, I.M. Cabrera, M.L. Granados, F. Kapteijn, J.L.G. Fierro, J. Catal. 239 (2006) 340–346.

[49] Q. Fu, S. Kudriavtseva, H. Saltsburg, M.F. Stephanopoulos, Chem. Eng. J. 93 (2003) 41–53.

[50] S. Scirè, S. Minicò, C. Crisafulli, S. Galvagno, Catal. Commun. 2 (2001) 229–232.

[51] P. Biswas, D. Kunzru, Int. J. Hydrogen Energy 32 (2007) 969–980.

[52] T. Tabakova, F. Boccuzzi, M. Manzoli, D. Andreeva, Appl. Catal., A 252 (2003) 385–397.

[53] C. Binet, M. Daturi, J.C. Lavalley, Catal. Today 50 (1999) 207–225.

[54] C.K. Costello, J.H. Yang, H.Y. Law, Y. Wang, J.N. Lin, L.D. Marks, M.C. Kung, H.H. Kung, Appl. Catal., A 243 (2003) 15–24.

[55] Y. Chen, J. Cheng, P. Hu, H. Wang, Surf. Sci. 602 (2008) 2828–2834.

[56] T. Shido, Y. Iwasawa, J. Catal. 141 (1993) 71–81.

[57] H. Sakurai, T. Akita, S. Tsubota, M. Kiuchi, M. Haruta, Appl. Catal., A 291 (2005) 179–187.

[58] A. El-Moemen, A. Karpenko, Y. Denkwitz, R.J. Behm, J. Power Sources 190 (2009) 64–75.

[59] S. Hilaire, X. Wang, T. Luo, R.J. Gorte, J. Wagner, Appl. Catal., A 215 (2001) 271–278.

[60] A. Karpenko, R. Leppelt, J. Cai, V. Plzak, A. Chuvilin, U. Kaiser, R.J. Behm, J. Catal. 250 (2007) 139–150.

[61] M. Mavrikakis, P. Stoltze, J.K. Nørskov. Catal. Lett. 64 (2000) 101–106.

[62] K. Qian, Z. Jiang, W. Huang, J. Mol. Catal. A: Chem. 264 (2007) 26–32.

[63] P.P.C. Udani, P.V.D.S. Gunawardana, H.C. Lee, D.H. Kim, Int. J. Hydrogen Energy 34 (2009) 7648–7655.

[64] A. Luengnaruemitchai, A. Kaengsilalai, Chem. Eng. J. 144 (2008) 96–102.

[65] M. Guisnet, P. Magnoux, Appl. Catal., A 212 (2001) 83–96.

[66] J.N. Armor, Appl. Catal., A 176 (2008) 159–176.

[67] L.I. Kongzhai, W. Hua, W. Yonggang, L. Mingchun, J. Rare Earths 26 (2008) 245–249.

[68] S. Kudo, T. Maki, T. Fukuda, K. Mae, Catalysts 1 (2011) 175–190.